

Cross-Correlation and Differential Technique Combination to Determine Displacement Fields

A. M. R. Sousa*, J. Xavier*, M. Vaz[†], J. J. L. Morais* and V. M. J. Filipe*

*CITAB, Engineering Department, University of Trás-os-Montes and Alto Douro, 5001-801 Vila Real, Portugal

[†]Faculty of Engineering, University of Porto, Porto, Portugal

ABSTRACT: This study presents a method to measure the displacement fields on the surface of planar objects with sub-pixel resolution, by combining image correlation with a differential technique. First, a coarse approximation of the pixel level displacement is obtained by cross-correlation (CC). Two consecutive images, taken before and after the application of a given deformation, are recursively split in sub-images, and the CC coefficient is used as the similarity measure. Secondly, a fine approximation is performed to assess the sub-pixel displacements by means of an optical flow method based on a differential technique. To validate the effectiveness and robustness of the proposed method, several numerical tests were carried out on computer-generated images. Moreover, real images from a static test were also processed for estimating the displacement resolution. The results were compared with those obtained by a commercial digital image correlation code. Both methods showed similar and reliable results according to the proposed tests.

KEY WORDS: *digital image correlation, displacement fields, optical flow, sub-pixel resolution*

Introduction

The measurement of the displacement field of an object from a sequence of images is a relevant information in many fields of digital image processing, such as motion estimation [1], image measurement [2] or image registration [3]. In the last decades, many techniques used in these fields became very important tools in the framework of experimental solid mechanics [4]. The major advantages of using optical methods, over point-wise measuring techniques, such as strain gauges, are the assessment of full-field data and their non-invasive nature. Besides, among other proposed full-field optical methods for displacement or strain measurement, such as grid methods [5, 6], interferometric moiré or speckle methods [7], image correlation requires relatively simple photo-mechanical set-up and preparation of the surface of specimens. In this technique, the displacement field is measured by following the deformation of a suitable textured pattern and is insensitive to vibration by means of post-processing/filtering [8], enabling the accurate extraction of surface displacement.

In digital image correlation (DIC) algorithms [9, 10], pixel level displacements between pairs of images are obtained searching the maximum value from the similarity of images regions. Either the sum of

absolute differences (SAD), the sum of squared differences (SSD) or the cross-correlation (CC) is usually used to evaluate the matching between regions [11, 12]. Greater resolution can be achieved when sub-pixel information is calculated increasing the accuracy of the displacement field measurement. There are a wide variety of algorithms performing this calculation [1], although they can be classified into four categories [3]: image interpolation, similarity interpolation, gradient-based and phase-correlation method. DIC was first proposed by Sutton and co-workers [12]. They used coarse-fine search to find the accurate displacements at pixel level, and the sub-pixel accuracy was achieved by combining the intensity pattern of an image with bilinear, polynomial or bi-cubic spline.

Currently, the existing tools using DIC still lack in information or present large errors over the calculated displacement fields in certain situations. These include for instance the processing of images captured from a specimen where a crack is present. In these cases, current methods using conventional DIC cannot deliver accurate information about the displacement fields near displacement discontinuities such as cracks or shear bands [13]. This is because of its window-based nature, i.e. each pixel contained in a certain processed sub-image will be given the same displacement value.

The underlying idea of this study is to propose a new DIC method combining well-known optical techniques such as image correlation and differential technique to calculate full-field displacements with sub-pixel accuracy. One major advantage of the proposed method is its full-field nature, i.e. each image pixel results in an individual displacement value. Therefore, this will enable the use of this method as the core of a new tool to investigate problems such as structural behaviour of fractured components with improved accuracy over the conventional DIC methods when dealing with displacements discontinuities. The method is based on a coarse-fine approach where a coarse pixel level displacement approximation is obtained by cross-correlation. At this stage, two consecutive images are recursively split into sub-images, and the CC coefficient is used as the similarity measure. In the second stage, a finer approximation is performed to obtain sub-pixel displacement calculated using an optical flow method [14–22] based on a differential technique.

In this early stage of development, the validation of the proposed method is accomplished by simple numerical analyses, which enable full control over the applied reference displacement field. These numerical tests consist of rigid-body translation and rotation tests, tensile and pure shear mechanical tests. Comparisons are necessary to validate proposed methodologies, so the obtained results are also compared to those measured by the commercial digital image correlation code GOM Aramis. The proposed method is explained in full detail in section 2. The effectiveness of the method is validated, and results are presented in section 3. Some conclusions and final remarks are addressed in section 4.

Proposed Method

The proposed method follows a 2-step coarse-fine approach: pixel level estimation (coarse) and sub-pixel level estimation (fine) of displacement fields. In the first step, the normalised cross-correlation is recursively applied over the sub-images obtained from the original images pair, using a quad-tree splitting process. In the second step, an optical flow method based on a differential technique is used. One of the constraints of optical flow is related with image intensity which must be nearly linear across a given period of time [23]. The direct application of optical flow to calculate the displacement fields on the surface of a specimen that undergoes a large deformation in a short period of time would introduce considerable errors in the resulting displace-

ment fields. Therefore, in the proposed method a first step is introduced to calculate the pixel level displacement of each sub-image. This procedure reduces to a minimum the pixel level displacement of each pixel inside a sub-image (after being shifted) fulfilling this way the optical flow constraint. This enables optical flow technique to perform accurate measurement of sub-pixel displacement.

Pixel level estimation

The pixel level displacement estimation is performed over a pair of images obtained before (reference) and after surface deformation (deformed). Using a quad-tree process each image is divided into a set of sub-images, and a normalised cross-correlation is applied to obtain the displacement of each sub-image centre point.

Cross-correlation

To perform this task each sub-image in the reference image is used to map another sub-image on the deformed image. The matching of a sub-image is found by maximising the normalised cross-correlation coefficient between intensity patterns of two sub-images

$$c(u, v) = \sum_{x,y} f(x, y) t(x - u, y - v) \quad (1)$$

in Equation (1) $c(u, v)$ is a measure of the similarity between the image f and the feature t . The process consists simply by moving the centre of the feature t , positioned at u, v , over each point x, y of image f . Among other disadvantages in using $c(u, v)$ for template matching, it can be noticed that the range of $c(u, v)$ is dependent on the size of the feature and is not invariant to changes in image amplitude, such as those caused by changing lighting conditions across the image sequence.

The correlation coefficient overcomes these difficulties by normalising the image and feature vectors to unit length, yielding a cosine-like correlation coefficient

$$\gamma(u, v) = \frac{\sum_{x,y} [f(x, y) - \bar{f}_{u,v}] [t(x - u, y - v) - \bar{t}]}{\{\sum_{x,y} [f(x, y) - \bar{f}_{u,v}]^2 \sum_{x,y} [t(x - u, y - v) - \bar{t}]^2\}^{0.5}} \quad (2)$$

where \bar{t} is the mean of pixels intensity of the feature and $\bar{f}_{u,v}$ is the mean of intensity $f(x, y)$ in the region under the feature. $\gamma(u, v)$ is referred as the *normalised cross-correlation* [24, 25].

Quad-tree image splitting

The image splitting is similar to a quad-tree division process and is used to enable coarse pixel level displacements estimation between reference and

deformed image, following a global to local approach. First, a global displacement between full-sized images is calculated using the correlation coefficient. Next, both images (reference and deformed) are submitted to the splitting process using a quad-tree technique which consists in dividing each one recursively into four (4) sub-images (Figure 1) and repeating for each pair the normalised cross-correlation calculation.

At any level n of the splitting process (Figure 2), the obtained displacement is assumed constant over the whole sub-image; notice that sub-image at level $n = 0$ represents the entire image. After the splitting process terminates, a coarse map of pixel level displacements between reference and deformed image is obtained from their sub-images.

The maximum number of splitting levels can be defined by:

$$n_{\max} = \log_2 \frac{\min_{l,c}}{2} \quad (3)$$

where

$$\min_{l,c} = \begin{cases} \text{lines,} & \text{lines} \leq \text{columns} \\ \text{columns,} & \text{columns} < \text{lines} \end{cases}, \quad (4)$$

(lines, columns) size of image

From Equation (3) the smallest sub-image size is given by:

$$s = \frac{\min_{l,c}}{2^n}, s \text{ must be an integer value} \quad (5)$$

The splitting process of a certain sub-image at level n stops when at least one of three conditions is satisfied: (1) the maximum number of splitting levels defined in Equation (3) is reached; (2) the displacement calculated from level n to level $n + 1$ does not follow a smooth behaviour; (3) or is the same. The expressions defining these conditions are expressed as follows:

$$(1) \quad m == n_{\max} \quad (6)$$

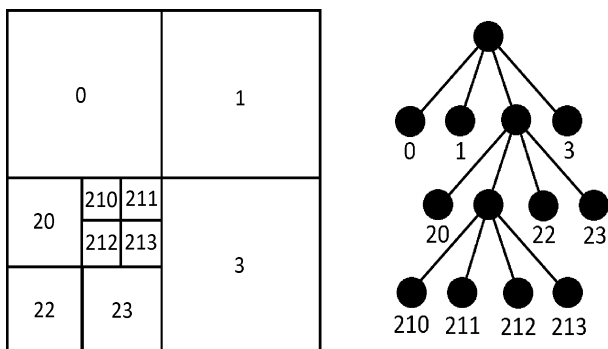


Figure 1: Quad-tree image splitting process

$$(2) \quad \text{abs}(d_{n+1} - d_n) > 1 \quad (7)$$

$$(3) \quad d_{n+1} == d_n \quad (8)$$

where m is the current splitting level of the method and d_n, d_{n+1} represents, respectively, the displacement of image at level n and $n + 1$.

Sub-pixel level estimation

After finding a coarse pixel level displacement between the two images, sub-pixel estimation is applied to obtain higher resolution. Each reference sub-image (resulting from the quad-tree decomposition) is shifted by their amount of pixel level displacement over the correspondent deformed sub-image. Next, the displacement estimation of each pixel belonging to the sub-image is computed using an optical flow technique (OF). The goal of OF is to compute an approximation to the 2D motion field – a projection of the 3D velocities of surface points onto the imaging surface – from spatiotemporal patterns of image intensity. The main stages of processing consist of the following: (1) pre-filtering or smoothing with low-pass/band-pass filters [to extract signal structure of interest and enhance SNR (signal-to-noise ratio)]; (2) the extraction of basic measurements such as spatiotemporal derivatives (to measure normal components of velocity); (3) the integration of the previously extracted measurements to produce a smooth 2D flow field. The method proposed in this article implements a first-order technique, more specifically, the local differential technique from Lucas & Kanade [15], which was proven to be efficient and reliable [23, 26].

Spatiotemporal derivatives

Differential techniques compute velocity from spatiotemporal derivatives of image intensity (I) or filtered versions of the image using low-pass or band-

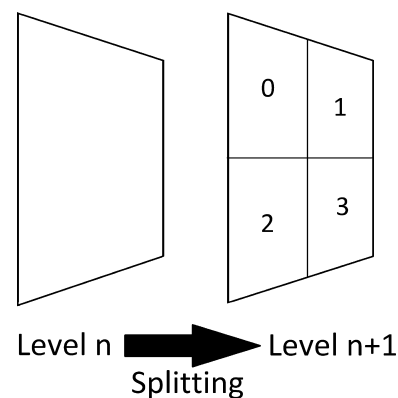


Figure 2: Splitting process at level n resulting in four sub-images

pass filters. In the present case a Gaussian filter is used. The main requirement for differential techniques is that $I(x, t)$ must be differentiable. The technique proposed by Lucas & Kanade implements weighted least-squares (LS) fit of local first-order constraints to a constant model for v in each small spatial neighbourhood Ω of position $x = (x, y)$, by minimising:

$$\sum_{x \in \Omega} W^2(x) [\nabla I(x, t) \cdot v + I_t(x, t)]^2, \quad (9)$$

A weighting function $W(x)$ is used to give more influence to constraints at the centre of the neighbourhood than at the periphery. Depending on the speckle size, this function could be adjusted to control the spatial resolution (i.e., the windows size). Gaussian functions are usually used for this purpose; however, other functions or weighting schemes can be used. $\nabla I(x, t)$ is the spatial intensity gradient, $\vec{v} \rightarrow (V_x, V_y)$ represents the two components image velocity and $I_t(x, t)$ is the partial time derivative of image intensity at position x in instant t . The displacement field resulting from differential technique has sub-pixel resolution usually with values < 1 pixel. For more details about equation terms and calculations, please refer to [23] or for a full detailed explanation and illustrative figures [14].

Estimation error cancellation

Sub-pixel displacements estimation includes a systematic error called “pixel-locking”. This error is such that estimated displacements d are greater than true values when $d < 0$, and less than true values when $d > 0$. This causes the histogram of the estimated values d to have peaks at integer pixel locations [27, 28].

In the proposed method to increase accuracy, this systematic error is cancelled using a technique first introduced by Shimizu and co-worker [27], called Estimation Error Cancellation (EEC). (Please refer to [28] for full details about the EEC method and the used features of the sub-pixel estimation error.)

The global displacement of each pixel is then obtained by adding its coarse pixel level displacement (cross-correlation) with the respective finer sub-pixel level displacement (differential technique). The resolution, i.e. how finer is the sub-pixel level displacement estimation, correspond, in turn, to the measurement error of the proposed method. This can be quantified analysing the displacement fields obtained when there is no observed movement of specimen between reference and analysed image. These analyses can be found in more detail in the static tests results included in this article (Experimental test).

Performance Assessment of the Proposed Method: Results and Discussion

Validation procedure

To assess the sensitivity and the accuracy of digital image correlation (DIC) methods, both numerical [26, 29] and experimental [30, 31] tests can be carried out. The underlying idea of these tests is to compare a known displacement field with the one calculated by DIC, when processing the images corresponding to two different configurations of the object under observation, taken before and after the applied transformation (Figure 3).

For the strict purpose of checking and validating a DIC method, it can be advantageous to process computer-generated speckle-pattern images [32]. In this approach, the numerical errors associated with the DIC method can be uncoupled from the experimental ones (e.g., light intensity variation, speckle pattern quality or error in applying an exact reference displacement). Moreover, more complex (e.g., heter-

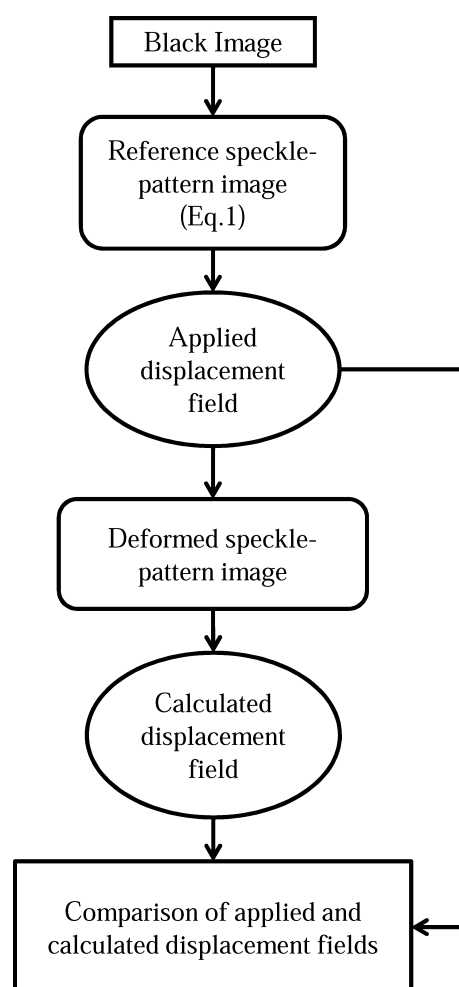


Figure 3: Flowchart representation of the computer-generated speckle-pattern images

ogeneous) deformation fields can be analysed, as experimentally only simple controlled tests such as static (motionless) or rigid-body tests (i.e., in-plane or out-of-plane translations and rotations) can be carried out.

One important issue when dealing with numerical tests is the generation and deformation of a realistic synthetic speckle-pattern image, *i.e.*, with a histogram and spectral properties similar to the ones of real speckle images which can be obtained, for example, by spray or airbrush painting [33]. Several authors [26, 34] have proposed analytical expressions for generating this type of synthetic images. The advantage is that an analytical displacement field can be straightforward applied to deform a given reference speckle-pattern image. Thus, images corresponding to undeformed (I_i) and deformed (I_f) configurations can be generated according to the following expressions:

$$I_i(x, y) = \sum_{k=0}^{N_s} I_k \exp \left\{ -\frac{(x - x_k)^2 + (y - y_k)^2}{R^2} \right\} \quad (10)$$

$$I_f(x, y) = \sum_{k=0}^{N_s} I_k \exp \left\{ -\frac{[x - U(x, y) - x_k]^2 + [y - V(x, y) - y_k]^2}{R^2} \right\}$$

where (x, y) are the pixel coordinates (corresponding to the sampled unit cells of the CCD sensor), (x_k, y_k) are the random positions of each speckle spot, I_k represent a random light intensity value defining the peak intensity of each speckle spot, R controls the size of the speckle spots, (N_s) is the total number of granular spots defining the speckle pattern, and $U(x, y)$ and $V(x, y)$ define the applied transformation corresponding to the displacement fields through the x and the y directions, respectively.

Images with a depth of 8 bit were considered in the numerical analyses. First, a pure black image was generated by initialising a $H \times V$ matrix filled with zero intensity light level, where H and V represent, respectively, the length and the width of the image –

this could correspond experimentally to cover the region of interest of a sample with black paint by means of a spray or airbrush for example. Secondly, the reference speckle-pattern image (undeformed configuration) was generated by iteratively adding images with a single randomly distributed grey scale spot characterised by a radius R and having a Gaussian distribution function – in practice, the resulting image could correspond to randomly spread white painting over the black background surface of the sample. The total number of spots (N_s) as well as their central location (x_k, y_k) within the spatial domain of the image, were randomly chosen. A sequence of images, corresponding to different deformed configurations, can then be generated, with regard to the reference speckle-pattern image, by applying an inverse displacement field (U_{app}, V_{app}) (Equation 10). Finally, a 5×5 Gaussian filter was applied to the generated images to obtain a smooth textured speckle pattern, which will represent a more realistic speckle image. In Figure 4 it is shown a speckle-pattern image, together with its histogram, which is typically generated from Equation (10) ($H = V = 1000$ pixels, $N_s = 6667$ spots, $R = 5$ pixels).

Numerical tests

In this work, the following numerical tests were carried out to quantify the performances of the proposed method: (1) in-plane translation test; (2) in-plane rotation test; (3) uniaxial tensile test; (4) pure shear test. For all these tests, the results obtained from the proposed method were also compared to those measured by the Aramis 6.02 GOM® software [35], by processing the same sequence of synthetic-generated images.

Rigid-body translation test

The in-plane rigid-body translation test is based on the analyses of a set of images generated by incrementally applying sub-pixel displacements to a reference image along one direction, *i.e.* $U(x, y) = u_0$.

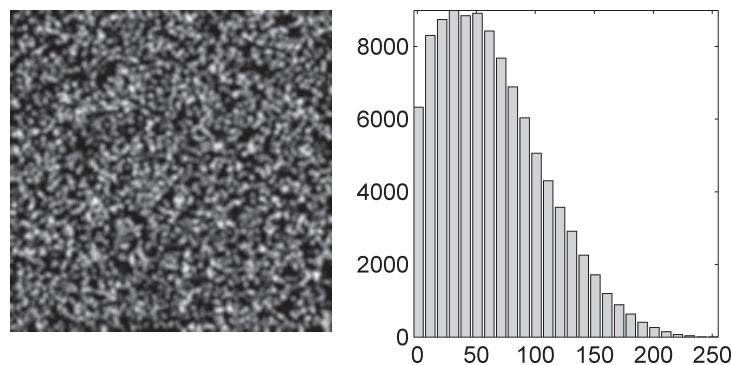


Figure 4: Typical generated speckle-pattern image and its histogram

Transformed images were then generated with regard to the reference one by cumulatively imposing a translation of 0.1 pixels in the x (column) direction up to 1 pixel (Equation (10), $H = V = 256$ pixels, $N_s = 1245$ spots, $R = 3$ pixels). These images were then processed by the proposed method as well as by the Aramis software. A differentiation window of 9×9 pixels and a subset size of 10×10 pixels were used in the proposed and Aramis methods, respectively, to resolve the granulometry of the speckle pattern and to guarantee an equivalent spatial resolution.

The comparison among the reference and both the proposed and the Aramis methods is shown in Figure 5A). As can be seen, the proposed method presents a higher precision than Aramis when comparing the obtained results with the reference applied translation. At each stage, a residual field was computed between the applied and the calculated displacements. From these noisy maps, the mean (systematic error) and standard deviation (random error) were evaluated; these results are shown in Figure 5B,C, respectively, as a function of the applied sub-pixel displacements. The mean bias error associated with both methods (Figure 5B) follows the typical sinusoidal variation with regard to the applied sub-pixel displacement, with values in the order of 10^{-3} of the pixel. The resolution (standard deviation), for the proposed method is, in general, better than Aramis and less than 4×10^{-3} of the pixel. These results validate the proposed method, according to this sub-pixel translation test.

Rigid-body rotation test

For the rigid-body rotation test, a set of images (Equation (11), $H = V = 256$ pixels, $N_s = 1245$ spots, $R = 3$ pixels) were generated by considering the following sequence of rotation angles: $\theta = \{0.005, 0.01, 0.015, 0.02, 0.04, 0.06, 0.08, 0.1, 0.15, 0.2, 0.4, 0.6, 0.8, 1.0\}$. The centre of rotation was chosen at the centre of the image. For the largest rotation angle of 1 degree the maximum displacements at the corners of the image were of about 5 pixels. These images were then processed by the proposed method (differentiation window of 9×9 pixels) as well as by the Aramis software (subset size of 10×10 pixels). The rotations applied to the images can be calculated from the displacement fields according to the following relationship:

$$U(x, y) = \theta y \quad V(x, y) = -\theta x \quad (11)$$

In Figure 6A it is shown the comparison among the reference and both the proposed and the Aramis methods. It can be seen that a relatively good agreement exist between the reference and both methods. In Figure 6B it is shown the mean bias error associ-

ated with the methods. In the Aramis code, the mean bias error seems rather constant with regard to the applied angle, and less than about 1% of the maximum imposed rotation. In the proposed method, the

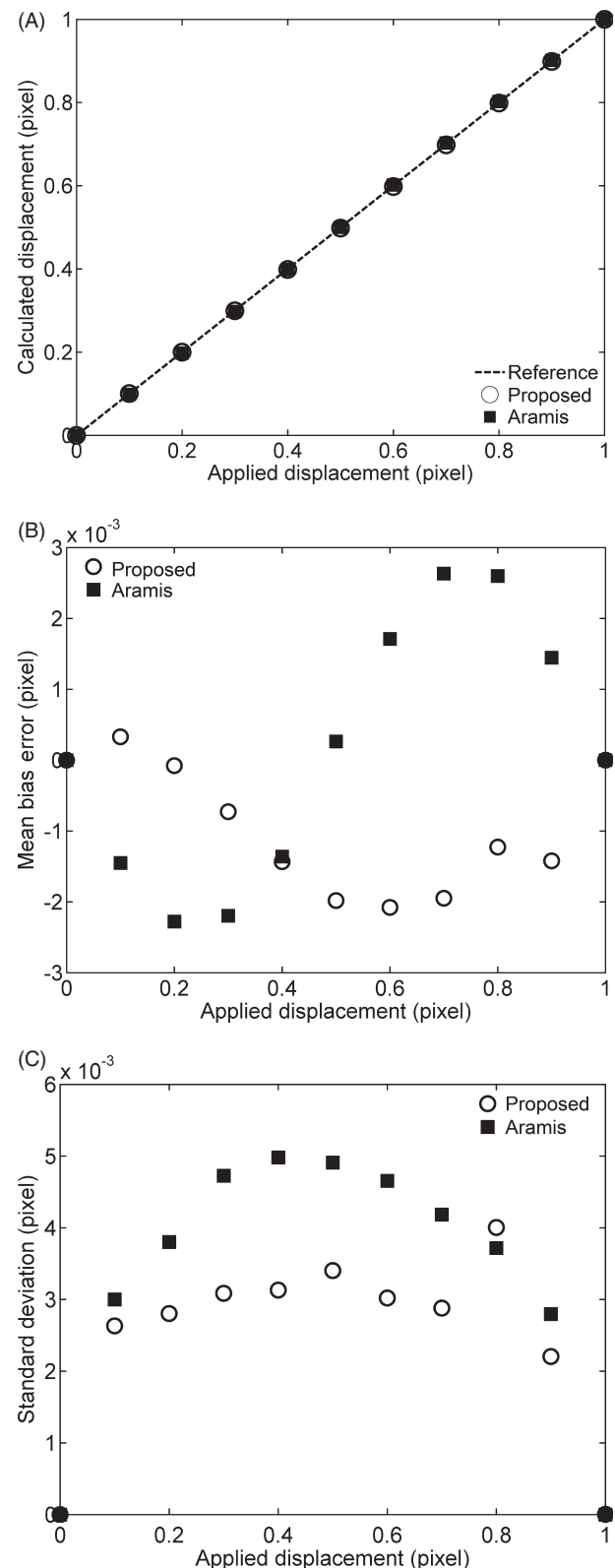


Figure 5: Rigid-body translation test: (A) calculated displacement, (B) mean bias error and (C) standard deviation as a function of the applied displacement – proposed (○) and aramis (■) methods; unit: pixel

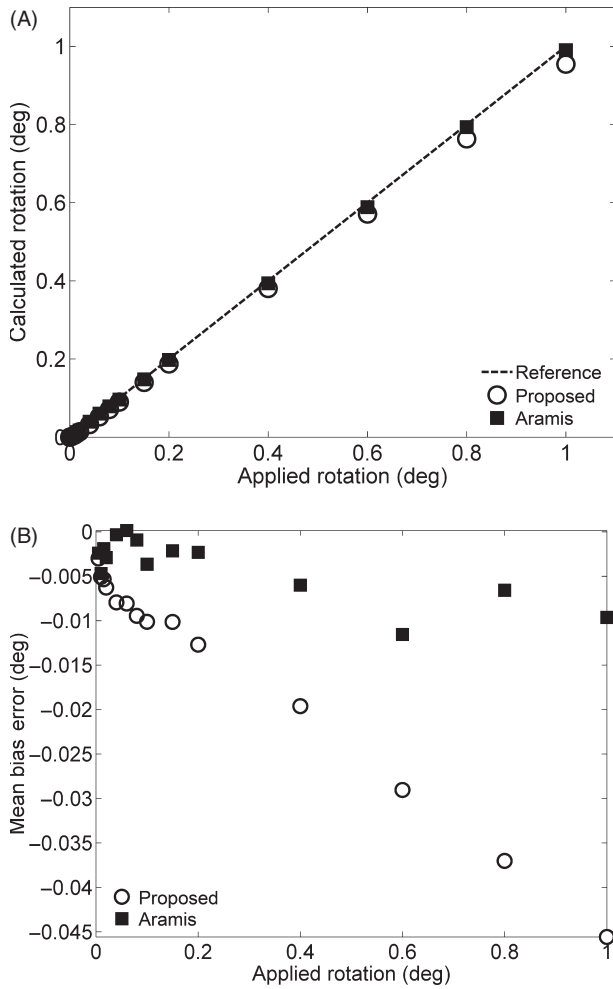


Figure 6: Rigid-body rotation test: (A) calculated displacement and (B) mean bias error as a function of the applied displacement – proposed (○) and aramis (■) methods; unit: pixel

bias error varies linearly with respect to the applied rotation angle; an error slightly higher than 4% of the maximum applied angle of rotation was measured.

Tensile mechanical test

The mechanical model of the uniaxial tensile test is presented in Figure 7A. The closed-form displacement field from this test can be obtained from the fundamental equations of solid mechanics (i.e., the equilibrium equations, the constitutive law under a plane stress approach and the strain-displacement relationship for small deformations). In the absence of rigid-body motion, this displacement field is given by:

$$U(x, y) = \frac{P}{E_{xx}A}x \quad \text{and} \quad V(x, y) = -\frac{\nu_{xy}P}{E_{xx}A}y \quad (12)$$

where E_{xx} , ν_{xy} are, respectively, the modulus of elasticity and Poisson's ratio of a given material, (A) is the cross-section area of the specimen and (P) is the global applied load.

As an example for the tensile test, a rectangular specimen with dimensions of $L = 200$ mm, $w =$

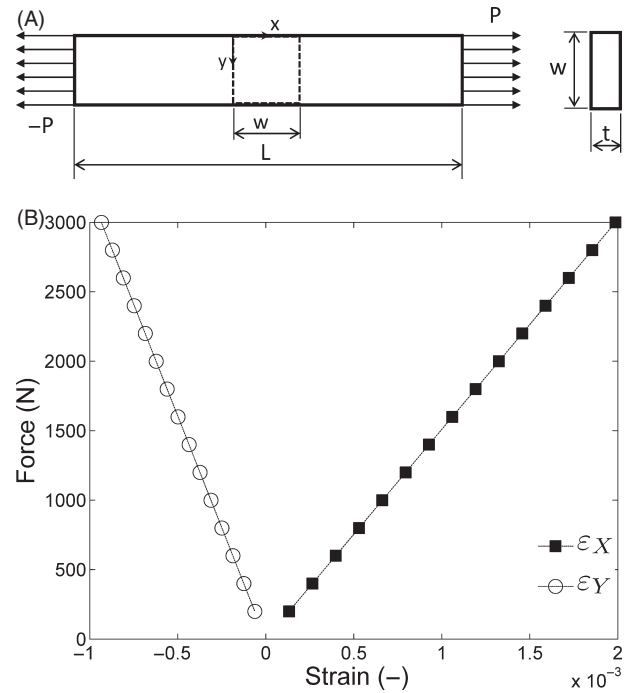


Figure 7: Uniaxial tensile test: (A) mechanical model; (B) Force (P) versus linear strains (ϵ_X , ϵ_Y) reference curve

20 mm and $t = 5$ mm was chosen (Figure 7A); this could correspond to a wooden sample oriented along its longitudinal direction of material symmetry [36]. A central region of 20×20 mm² was considered, which could correspond experimentally to the region of interest for image grabbing. The reference elastic properties input into Equation 12 were of *P. pinaster* wood determined experimentally from tensile tests [36]: $E_{xx} = 15.1$ GPa and $\nu_{xy} = 0.47$. A reference speckle-pattern image was initially obtained from Equation 10, from which $H = V = 1000$ pixels, $N_s = 6667$ spots, and $R = 5$ pixels. Finally, by taking into account the analytical displacement fields in Equation 12, several deformed images were generated, by increasing the applied load (P) from 200 up to 3000 N with increments of 100 N. A load versus the linear strains reference curve was thus obtained as shown in Figure 7B. This is the typically information measured experimentally on this test method.

As an example, the reference U and V displacement fields (Equation 12), together with the calculated displacements from the proposed (I) and the ARAMIS (II) methods, as well as the residual maps obtained from the differences between both are plotted in Figure 8 for the load of 200 N (Figure 7). As can be seen, namely from the residual maps between the reference and calculated fields, both methods can reproduce relatively well the applied displacement fields.

These displacement fields were then processed to determine the strain fields. As the vector fields

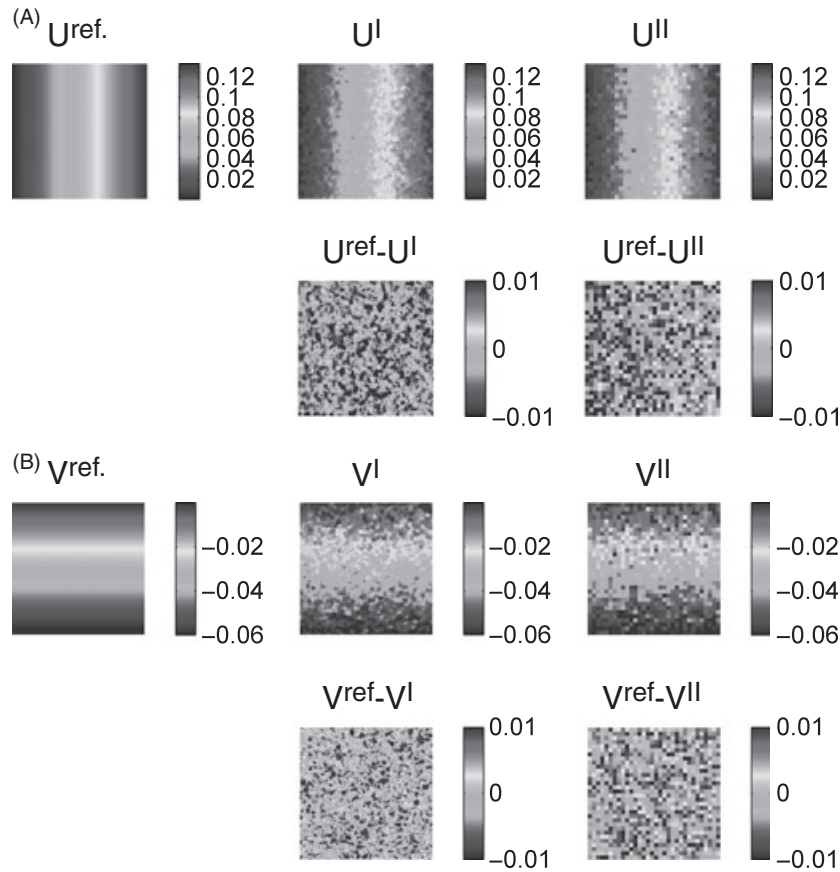


Figure 8: (A) Reference (*ref*), (B) calculated (*I* = proposed method; *II* = ARAMIS DIC2D[®]) and (C) residual displacement maps: (1) *U* and (2) *V* (*ref*: $F = 200$ N, $\varepsilon_x = 1.325 \times 10^{-4}$, $\varepsilon_y = -6.225 \times 10^{-5}$)

involved in this test are smooth, a global approximation scheme using least-square polynomial regression was chosen for the reconstruction of the uniform strain fields [6]. These strain fields, determined from the displacement fields measured by the proposed and the ARAMIS DIC2D methods, together with the applied load and geometry of the sample, were then used to plot the stress-strain ($\sigma_x - \varepsilon_x$) and strain-strain ($\varepsilon_y - \varepsilon_x$) curves (Figure 9), typical from this type of test. As can be seen, both the mechanical responses follow closely the reference one. From these plots, the elastic engineering parameters, E_{xx} and ν_{xy} (Equation 12), were determined by linear regression, as it is usually performed when processing experimental data. The results obtained with this procedure are summarised in Table 1, and compared with the reference values, used to generate the applied displacement fields (Equation 12). As it can be concluded, both methods could retrieve the reference material properties with a relative difference less than 1%.

Pure shear mechanical test

The mechanical model of the pure shear test is presented in Figure 10A. The closed-form displacement field of this test can be given as:

$$U(x, y) = \frac{P}{(A * G_{xy})} * y \quad V(x, y) = \frac{P}{(A * G_{xy})} * x \quad (13)$$

where G_{xy} is the shear modulus of a material, (A) is the cross-section area of the specimen and (P) is the global applied load.

A region of interest with $l = w = 10$ mm and a thickness of 5 mm was considered in this numerical test (Figure 10A). A shear modulus of *P. pinaster* wood of $G_{xy} = 1.1090$ GPa [36] was chosen as reference value (Equation 13).

Generated speckle images were obtained from Equation 10 by choosing $H = V = 1000$ pixels, $N_s = 6667$ spots and $R = 5$ pixels. Several deformed images were then generated by incrementally applying a load (P) from 100 up to 1000 N, as shown in Figure 10B, where the load is plotted as a function of the shear strains.

The same sequence of generated images was then processed with both methods to estimate the applied displacement fields. These displacement fields were then processed to determine the strain fields. For the proposed method a global approximation scheme using least-square polynomial regression was chosen for the reconstruction of the strain field [6]. From these data, the stress-strain ($\tau_{xy} - \gamma_{xy}$) curve was

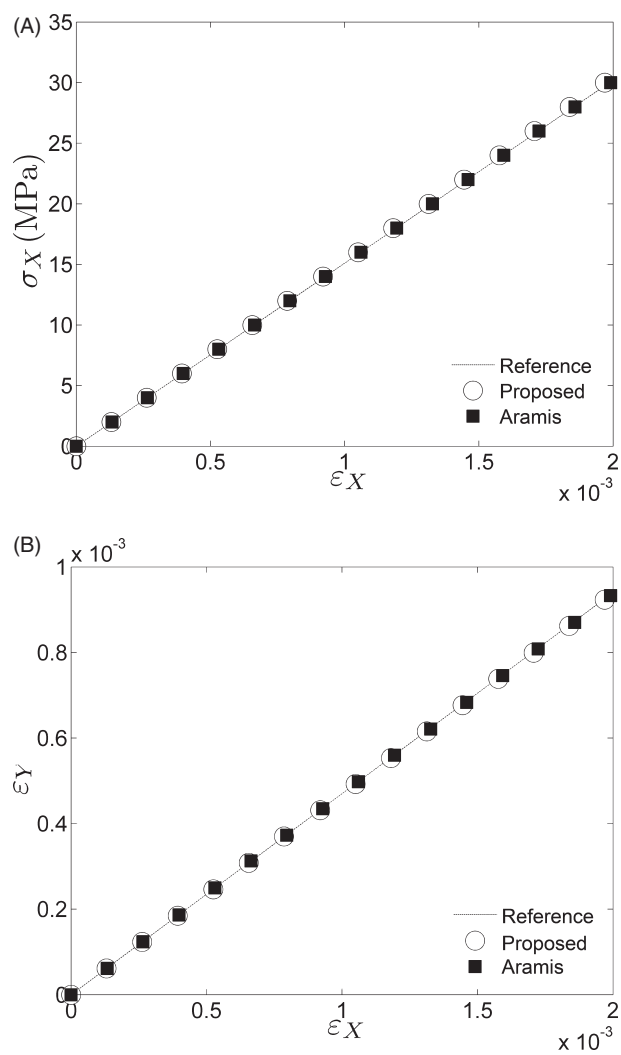


Figure 9: (A) X stress–X strain and (B) Y strain–X strain curves of the in the simulated uniaxial tensile test measured by the proposed (○) and Aramis (■) methods

plotted, in Figure 11, which shows that the mechanical response measured from both methods follow relatively well the reference one. From these plots, the shear modulus was determined by least-square regression, as it is usually performed when processing experimental data. The results obtained with this procedure are summarised in Table 2, and compared with the reference values, used to generate the applied displacement fields (Equation 13). As it can be concluded, both methods could retrieve the

Table 1: Elastic engineering properties measured from the uniaxial tensile test

	E_{xx} (MPa)	ν_{xy}
Reference	15100	0.470
Proposed method	15229 (0.86%)	0.469 (−0.30%)
Aramis DIC-2D	15072 (−0.19%)	0.469 (−0.28%)

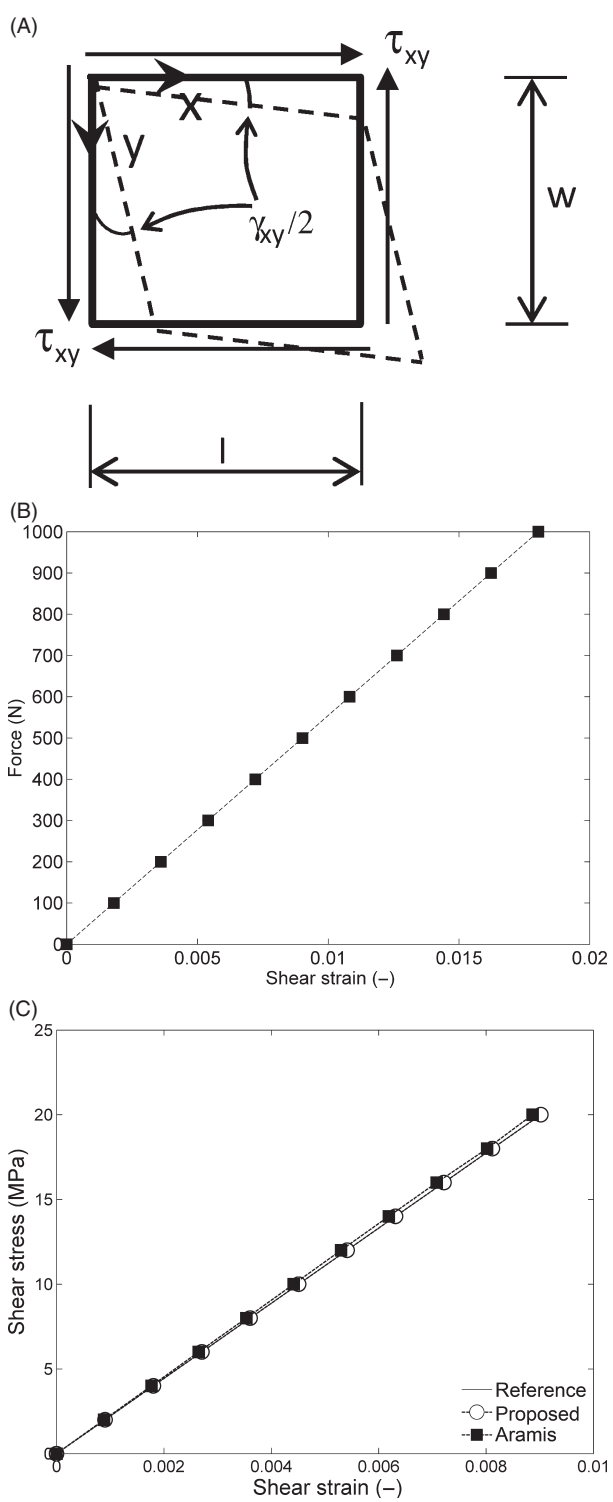


Figure 10: Pure shear test: (A) mechanical model; (B) Force (P) versus linear strains (ϵ_X , ϵ_Y) reference curve; (C) shear stress–strain curve measured by the proposed (○) and Aramis (■) methods

reference material properties with good estimation. It must be pointed out that some difference between the reference and calculated values reported in Table 2 could also be attributed to the numerical differentiation of the displacement fields.

Experimental test

In the previous section, numerical tests were analysed for the validation of the proposed method. To complement these analyses, a static motionless test is proposed here, by processing real speckle-pattern images (Figure 11A). This test consists in taking several images of a reference region, without any applied deformation. Therefore, the reference displacement fields in this case will be zero. This set of images was then processed by the proposed and Aramis methods to compute the displacement fields. Typically, noisy displacement fields are measured, from which the displacement resolution can be assessed by statistical analysis. The mean and standard deviation of this noisy signal will globally quantify the mean bias error and accuracy of the methods, respectively. This study is summarised in Figure 11B. As it can be seen, both methods show similar results in terms of global error measurements.

Conclusions

Currently the existing tools, either commercial or developed by investigators still lack in information or present large errors over the calculated displacement fields near displacement discontinuities such as cracks or shear bands. In this work a method combining cross-correlation and a differential technique was proposed, allowing the measurement of displacement fields in each pixel of the image with sub-pixel accuracy. This method will be used, in future work, as the core of a new tool to investigate problems such as structural behaviour of fractured components dealing with displacements discontinuities.

The work presented in this article included the description of the developed method which is based on a coarse-fine approach. A coarse approximation is first performed using a pixel level estimation (cross-correlation), followed by a fine measurement by a sub-pixel level estimation approach (differential technique). Because no local interpolation of the discrete grey level distribution is required, the proposed method can be eventually applied, in the future, to a wider range of textured patterns.

In this early stage of development the validation of proposed method was accomplished by numerical analysis, which enabled full control over the experiments and the expected displacement fields output were used as reference for comparison. It was also used a commercial software ARAMIS DIC-2D® as a reference for accuracy comparison with the proposed

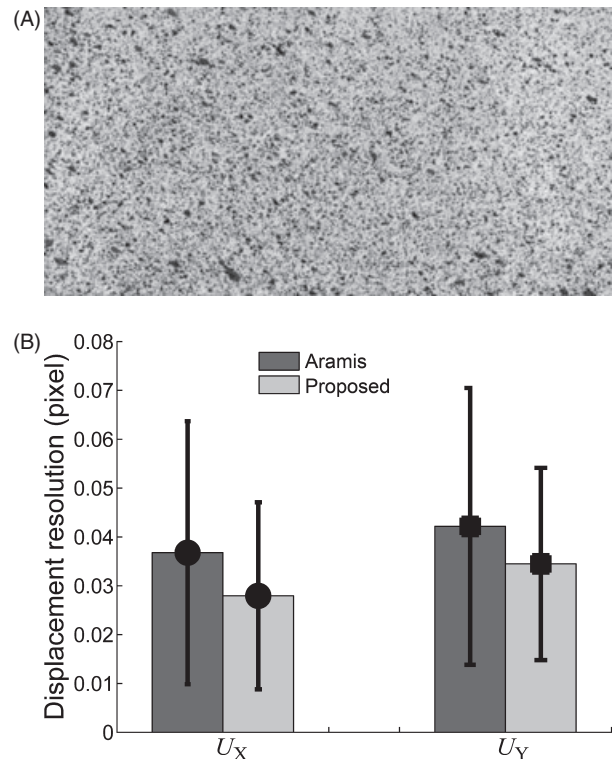


Figure 11: Static motionless test: (A) real speckle-pattern image, (B) displacement resolution measured by the proposed and Aramis methods (unit: pixel).

method. To validate the proposed method, four types of numerical tests were carried out: (1) in-plane translation test; (2) in-plane rotation test; (3) uniaxial tensile test; (4) pure shear test. The analytical known displacement fields were then compared to those calculated by the proposed method and the ARAMIS-DIC2D GOM® code. Both methods showed similar and reliable results using numerical tests. In the case of rigid-body translation test the proposed method presented a higher precision than commercial software Aramis when comparing the obtained results with the reference applied translation. The mean (systematic error) and standard deviation (random error) were also evaluated and the proposed method showed, in general, a lower error. Furthermore, static motionless tests with real speckle-pattern images were also analysed. Again both methods showed similar results in terms of the estimation of the global displacement resolution.

Table 2: Shear modulus measured from the pure shear test

	G_{xy} (MPa)
Reference	1.1090
Proposed method	1.1264 (1.57%)
Aramis DIC-2D	1.1089 (−0.008%)

The requirements of the proposed method are that displacement fields have to be obtained from textured images/surfaces with spray paint or natural texture in a way that correlation/matching is possible between reference and displaced image. The limitations, in its current state of development, can be pointed as dealing with big rotations which can result in loss of accuracy in the obtained displacement fields. Also, the proposed method is not prepared for real time processing at this stage of development.

The features of proposed method along with the quality of obtained results from numerical tests are encouraging and will enable, in future work, its refinement and use it as a mean to characterise a wide range of materials and their behaviour (e.g. structural behaviour of fractured objects under load).

REFERENCES

- Aggarwal, J.K. and Nandhakumar, N. (1988) On the Computation of Motion from Sequences of Images – a Review. *Proc. IEEE* **76**, 917–935.
- West, G.A.W. and Clarke, T.A. (1990) A Survey and Examination of Subpixel Measurement Techniques. *Proc SPIE: Close-Range Photogram. Meets Mach. Vis.* **1395**, 456–463.
- Tian, Q. and Huhns, M.N. (1986) Algorithms for Subpixel Registration. *Comput. Vis. Graph. Image Process.* **35**, 220–223.
- Sutton, M.A., Orteu, J.-J. and Schreier, H. (2009) *Image correlation for shape, motion and deformation measurements: Basic concepts, theory and applications*, Springer, New York.
- Surrel, Y. (1999) Fringe analysis. In: *Photomechanics (Topics in Applied Physics)* (P.K. Rastogi, Ed.). Springer Verlag, Germany: 57–104.
- Xavier, J., Avril, S., Pierron, F. and Morais, J. (2007) Novel experimental approach for longitudinal-radial stiffness characterisation of clear wood by a single test. *Holzforschung*, **61**, 573–581.
- Cloud, G.L. (1995) *Optical methods of engineering analysis*. Cambridge University Press, New York.
- Yaofeng, S., Meng, T.Y., Pang, J.H.L. and Fei, S. (2005) Digital Image Correlation and its Applications in Electronics Packaging. *Proc. 7th Electron. Packag. Technol. Conf. (EPTC2005)* **1**, 129–134.
- Peters, W.H. and Ranson, W.F. (1982) Digital image techniques in experimental stress analysis. *Opt. Eng.* **21**, 427–432.
- Sutton, M.A., Wolters, W.J., Peters, W.H., Ranson, W.F. and McNeil, S.R. (1983) Determination of displacements using an improved digital image correlation method. *Image Vis. Comput.* **1**, 133–139.
- Hill, P.R., Chiew, T.K., Bull, D.R. and Canagarajah, C.N. (2006) Interpolation Free Subpixel Accuracy Motion Estimation. *IEEE Trans. Circ. Syst. Video Technol.* **16**, 1519–1526.
- Chu, T.C., Ranson, W.F., Sutton, M.A. and Peters, W.H. (1985) Applications of Digital Image Correlation Techniques to Experimental Mechanics. *Exp. Mech.* **25**, 232–244.
- Poissant, J. and Barthelat, F. (2009) A Novel “Subset Splitting” Procedure for Digital Image Correlation on Discontinuous Displacements Fields. *Exp. Mech.* **50**, 353–364.
- Horn, B.K.P. and Schunk, B.G. (1981) Determining optical flow. *Artif. Intell.* **17**, 185–2003.
- Lucas, B. and Kanade, T. (1981) An iterative image registration technique with an application to stereo vision. *Proc. DARPA IU Workshop*, 121–130.
- Nagel, H.H. (1983) Displacement vectors derived from second-order intensity variations in image sequences. *CGIP*, **21**, 85–117.
- Uras, S., Girosi, F., Verri, A and Torre, V. (1988) A computational approach to motion perception. *Biol. Cybern.*, **60**, 79–97.
- Anandan, P. (1987) *Measuring Visual Motion from Image Sequences*. PhD dissertation, COINS TR 87-21, Univ. of Massachusetts, Amherest, MA.
- Singh, A. (1990) An estimation-theoretic framework for image-flow computation. *Proc. IEEE ICCV*, 168–177.
- Heeger, D.J. (1987) Model for the extraction of image flow. *J. Opt. Soc. Am.*, **A4**, 1455–1471.
- Waxman, A.M. and Wohn, K. (1985) Contour evolution, neighbourhood deformation and global image flow: Planar surfaces in motion. *Int. J. Rob. Res.*, **4**, 95–108.
- Fleet, D.J. and Jepson, A.D. (1990) Computation of component image velocity from local phase information. *Int. J. Comput. Vis.*, **5**, 77–104.
- Barron, J.L., Fleet, D.J. and Beauchemin, S.S. (1994) Performance of Optical Flow Techniques. *IJCV*, **12**, 43–77.
- Lewis, J.P. (1995) Fast Normalized Cross-Correlation, In Vision Interface. *Canad. Image Process. Pattern Recognit. Soc.*, 120–123.
- Haralick, R.M. and Shapiro, L.G. (1992) *Computer and Robot Vision*. Addison-Wesley Longman Publishing Co., Inc., Boston, MA, USA, 316–317.
- Pan, B., Xie, H.-M., Xu, B.Q. and Dai, F.L. (2006) Performance of sub-pixel registration algorithms in digital image correlation. *Meas. Sci. Tech.*, **17**, 1615–1621.
- Shimizu, M. and Okutomi, M. (2001) Precise sub-pixel estimation on area-based matching. *Proc. 8th IEEE Int. Conf. Comput. Vis. ICCV'01* **1**, 90–97.
- Shimizu, M. and Okutomi, M. (2006) Multi-Parameter Simultaneous Estimation on Area-Based Matching. *Int. J. Comput. Vis.*, **67**, 327–342.
- Lecompte, D., Smits, A., Bossuyt, S., Sol, H., Vantomme, J., Van Hemelrijck, D. and Habraken, A.M. (2006) Quality assessment of speckle patterns for digital image correlation. *Opt. Lasers Eng.* **44**, 1132–1145.
- Wang, Y. and Cuitino, A.M. (2002) Full-field measurements of heterogeneous deformation patterns on polymeric foams using digital image correlation. *Int. J. Solids Struct.*, **39**, 3777–3796.
- Haddadi, H. and Belhabib, S. (2008) Use of rigid-body motion for the investigation and estimation of the measurement errors related to digital image correlation technique. *Opt. Lasers Eng.* **46**, 185–196.

32. Bornert, M. (2007) *Évaluation métrologique d'algorithmes de corrélation d'images numériques*. 18ème Congrès Français de Mécanique, Grenoble: 27–31 août.
33. Orteu, J.-J., Garcia, D., Robert, L. and Bugarin, F. (2006) A speckle-texture image generator. In: *Proceedings of SPIE, the International Society for Optical Engineering*, vol. 6341 (P. Slangen and C. Cerruti, Eds.) International Society for Optical Engineering, Nimes: 63410H.1–63410H.6.
34. Wattrisse, B., Chrysochoos, A., Muracciole, J.-M. and Némoz-Gaillard, M. (2001) Analysis of strain localization during tensile tests by digital image correlation. *Exp. Mech.* **41**, 29–39.
35. ARAMIS commercial software. GOM, (<http://www.gom.com/>).
36. Pereira, J.L. (2005) *Comportamento mecânico da madeira em tracção nas direcções de simetria material*. M.Sc. Thesis, University of Trás-os-Montes e Alto Douro, Vila Real, (in Portuguese).